

# Replication of Apparent Nonlinear Seismic Response with Linear Wave Propagation Models

Daniel R. H. O'Connell

It is necessary to understand ground-motion amplification by sediment, defined as the ratio of ground motions at sediment sites to those at rock sites, to predict seismic loadings for earthquake engineering. At sediment sites, observed weak-motion amplifications from magnitude 3 to 4 aftershocks of the 1994 Northridge earthquake were twice as large as magnitude 6.7 mainshock amplifications. Amplitude-dependent (nonlinear) amplification by sediment is one explanation. However, earthquake simulations with empirical impulse responses and elastic finite-difference calculations with weakly heterogeneous, random three-dimensional (3D) crustal velocity variations show that linear wave propagation can explain observed (apparently nonlinear) sediment responses. Random 3D velocity variations also reproduce the observed log-normal dispersion of peak ground motions. Deterministic wave propagation models are not adequate to quantify the scaling and dispersion of near-source ground motions.

Strong ground-motion information (estimates of peak amplitudes, durations, and phasing of seismic waves) is necessary to engineer earthquake-resistant buildings and critical structures, such as dams, bridges, and lifelines. Empirical ground-motion attenuation relations provide peak horizontal acceleration (PHA) and response spectra but rely on relatively sparse near-source ground-motion data, particularly for magnitude ( $M$ ) > 6.7 earthquakes on reverse or normal faults (1). Fault rupture simulations with deterministic, one-dimensional (1D), flat-layered velocity model impulse responses,  $G_{1D}$ , have been used to quantify the effects of rupture directivity on peak horizontal velocity (PHV) near faults for periods ( $T$ ) > 1 s (2) and PHV and PHA for  $T > 0.1$  s (3). Simulations of a  $M$  7.0 blind-thrust earthquake beneath the Los Angeles basin with  $G_{1D}$  responses for  $T > 1$  s suggest that PHVs of 150 to 200 cm/s may occur above the fault (2). Although these results appear consistent with observed near-source PHVs, PHVs exceeding 130 cm/s for  $T > 1$  s have not been observed, even for the  $M$  7.3 Landers and  $M$  7.4 Tabas earthquakes.

The idealized symmetries in 1D crustal velocity models used to generate  $G_{1D}$  responses do not contain correlated-random (4) 3D velocity heterogeneity shown to exist throughout the crust (5) and the mantle (6). Weak (~5% standard deviation,  $\sigma$ ), random fractal crustal velocity variations are required to explain observed body-wave travel-time variations and high-frequency seismic coda waves (5). The velocity bias between velocity

models of Earth derived from short-period body waves and those derived from free oscillations is explained by 1%  $\sigma$  random relative velocity fluctuations in the mantle (6). Theoretical 1D site corrections and scattering functions are sometimes used to represent effects of 3D velocity heterogeneity (7). Empirical impulse responses from small earthquakes provide an alternative approach to synthesize ground motions (8), but often the number of available empirical responses is insufficient to represent the amplitude, phase, and radiation pattern variations that occur in the near-source region of a large fault rupture.

Ground-motion amplifications at alluvial sites during the 17 January 1994  $M$  6.7 Northridge earthquake were about two times less than amplifications of these sites estimated from the aftershocks (9). Nonlinear soil amplification has been proposed to explain these observations (9, 10). Here, empirical and theoretical approaches show that linear wave propagation through random crustal velocity structure can reproduce apparent nonlinear amplification at sediment sites during

the Northridge earthquake and that random crustal velocity variations can have a substantial effect on the scaling and dispersion of near-source PHV and PHA.

## Combined Theoretical-Empirical Site-Response Modeling

At a recording site with a crustal velocity structure typical of most thin alluvial sites in southern California (11), deterministic  $G_{1D}$  synthetic waveforms fail to reproduce observed amplitude and phase variations of near-source ground motions from microearthquakes for  $0.1 \text{ s} < T < 4 \text{ s}$ . Synthetic  $G_{1D}$  waveforms only partially reproduce short portions of the microearthquake direct  $S$  waveforms. To improve synthetic waveforms, I applied site-specific scattering functions, derived from nine microearthquake waveforms recorded at the site, to  $G_{1D}$ . Wave-shaping filters,  $W$ , were calculated to extract 2.5- to 3-s site-specific scattering functions ( $C$ ) from waveform windows behind the first one to two cycles of the direct  $S$  waves (12). Theoretical-empirical responses,  $G_{\text{site}}$ , were obtained by convolving  $C$  with  $G_{1D}$ .

The ability of  $G_{\text{site}}$  responses to reproduce PHVs and PHAs from the 1994 Northridge earthquake was evaluated with earthquake simulations. An initial fault rupture model was developed, and nine iterations of forward modeling were used to find a single rupture model that fits strong motion data at stations RSS, SYL, NHL, U56, and PARD for  $T > 0.1$  s with  $G_{\text{site}}$  responses (13).  $G_{\text{site}}$  synthetic waveforms reproduce observed PHVs and PHAs from all five stations with minimal biases (Table 1), including stations RSS and SYL, which experienced the largest PHVs associated with rupture directivity (Fig. 1). In contrast,  $G_{1D}$  synthetic waveforms overpredicted observed Northridge amplitudes in the 0.5- to 3-Hz range by a factor of 1.82 (Table 1), consistent with estimates of Northridge aftershock-to-mainshock amplification ratios of ~2 in this frequency range (9). Thus, reduced coherency in the summation of direct  $S$  waves due to complex linear wave propagation responses ( $G_{\text{site}}$ ) can explain observed mainshock deamplification at sediment sites

**Table 1.** Observed (Obs.) and  $G_{\text{site}}$  synthetic Northridge PHV and PHA at five stations updip from the hypocenter. Mean  $G_{1D}/G_{\text{site}}$  ratios are the smoothed spectral ratios of  $G_{1D}$ -to- $G_{\text{site}}$  synthetic ground motions averaged over the 0.5- to 3-Hz frequency band.

Station	Obs. PHV (cm/s)	$G_{\text{site}}$ PHV (cm/s)	$G_{\text{site}}$ PHV bias (%)	Obs. PHA (cm/s <sup>2</sup> )	$G_{\text{site}}$ PHA (cm/s <sup>2</sup> )	$G_{\text{site}}$ PHA bias (%)	Mean $G_{1D}/G_{\text{site}}$ ratio (0.5 to 3 Hz)
RSS	173	161	7	873	806	8	1.58
SYL	132	128	3	848	1067	-26	1.92
NHL	121	110	10	735	888	-21	1.73
U56	94	102	-8	458	371	19	2.27
PARD	76	82	-9	696	511	27	1.58
Mean			0.4			1.4	1.82

U.S. Bureau of Reclamation, Box 25007 D-8330, Denver, CO 80225, USA. E-mail: geomagic@seismo.usbr.gov

during the Northridge earthquake, and non-linear sediment responses are not required. Although  $G_{1D}$  and  $G_{site}$  synthetic waveforms reproduce microearthquake PHVs and PHAs, only  $G_{site}$  synthetic waveforms also reproduce Northridge mainshock PHVs and PHAs at sediment sites (14). Jarpe and Kasameyer (15) used combined theoretical-empirical impulse responses to reproduce ground motions at rock and stiff-soil sites from the 1989 M 6.9 Loma Prieta earthquake and showed that nonlinear site effects were not required. Thus, empirical analyses of linear wave propagation complexity explain the inability of 1D synthetic modeling approaches (9) to replicate apparent nonlinear amplifications at sediment sites.

To further evaluate the impact of using em-

pirical site responses in earthquake simulations, I calculated synthetic ground motions for a maximum directivity, hanging-wall site above a M 6.9 reverse-faulting earthquake (16). A common set of kinematic rupture models was used with both  $G_{site}$  and  $G_{1D}$  responses. Deterministic  $G_{1D}$  simulations predicted a median PHA 35% larger, a median PHV 64% larger, and a population of extreme PHAs and PHVs larger than those of the  $G_{site}$  simulations.  $G_{site}$  and  $G_{1D}$  PHVs have strikingly different amplitude-period responses. At this site, synthetic  $G_{site}$  PHVs, both for  $T > 1$  s and  $T < 1$  s, are similar to observed near-source PHVs but do predict a small probability (5%) of exceeding maximum PHVs observed to date. Conversely, 8.5% of the  $G_{1D}$  PHVs were greater than 1.5 times the largest PHVs observed to date.

### Random 3D Crustal Velocity Variations and Ground-Motion Scaling

Random variations of crustal velocity and complex 3D near-surface velocity structure are two physical factors that contribute to the complexity of direct  $S$ -wave responses. Hence, detailed near-surface velocity modeling can improve synthetic fits to observed seismograms (17), and theoretical scattering functions can make synthetic strong motions more realistic (7). Multiple-scattering theory shows that the scattered wave field becomes progressively dominated by  $S$  waves during propagation through heterogeneous regions (18). Quantifying the effects of 3D velocity heterogeneity on direct  $S$  waves is necessary to understand the influence of random crustal velocity variations on the scaling of near-source ground motions.

Frankel and Clayton (5) investigated Gaussian, exponential, and self-similar fractal correlation models of random spatial variations of crustal seismic velocities with two-dimensional (2D) elastic finite-difference calculations. They found that only fractal, self-similar velocity fluctuations with an autocorrelation function,  $P$ , of the form

$$P(k_r) \approx \frac{a^n}{1 + (k_r a)^n} \quad (1)$$

where  $a$  is the correlation distance,  $k_r$  is the radial wave number, and  $n = 2$  in 2D, reproduced short-period ( $T < 1$  s) body-wave travel-time variations, coda amplitudes, and coda durations for ground motions recorded over length scales of tens of kilometers to tens of meters. Self-similar distributions of slip velocity on faults reproduce the observed frequency-squared, high-frequency spectral amplitude decay of earthquakes (19) and the commonly observed  $b$  value of 1 (20). Analyses of the spectral properties of primary shallow crustal reflection coefficients (21) allow values of  $n$  that range from 1.5 (weaker correlation and more jagged media) to 4 (stronger correlation and smoother media). In 3D, with  $n = 3$ , the standard deviation of random variations,  $\sigma$ , is independent of  $k_r$  (or length scale) for  $k_r a \gg 1$  and the medium is self-similar (5). In 3D,  $n = 2$  provides a fractal medium that displays irregularity at all length scales, but with  $\sigma$  proportional to  $k_r$  for  $k_r a \gg 1$ , consistent with shallow velocity variations at southern California alluvial and soft rock sites (11). Consequently,  $n = 2$  is used in Eq. 1 to construct 3D models of random velocity variations in the upper 5 km of the crust.

An elastic, 3D, finite-difference approach (22) was used to calculate free-surface ground motions produced by propagation of vertically incident, uniform-amplitude  $SV$  plane waves through a fractal upper crust with  $a = 1$  km and  $\sigma = 5\%$  (Fig. 2). Values of  $1 \text{ km} < a < 10 \text{ km}$  may be realistic for the shallow crust in compressive tectonic areas such as the Transverse

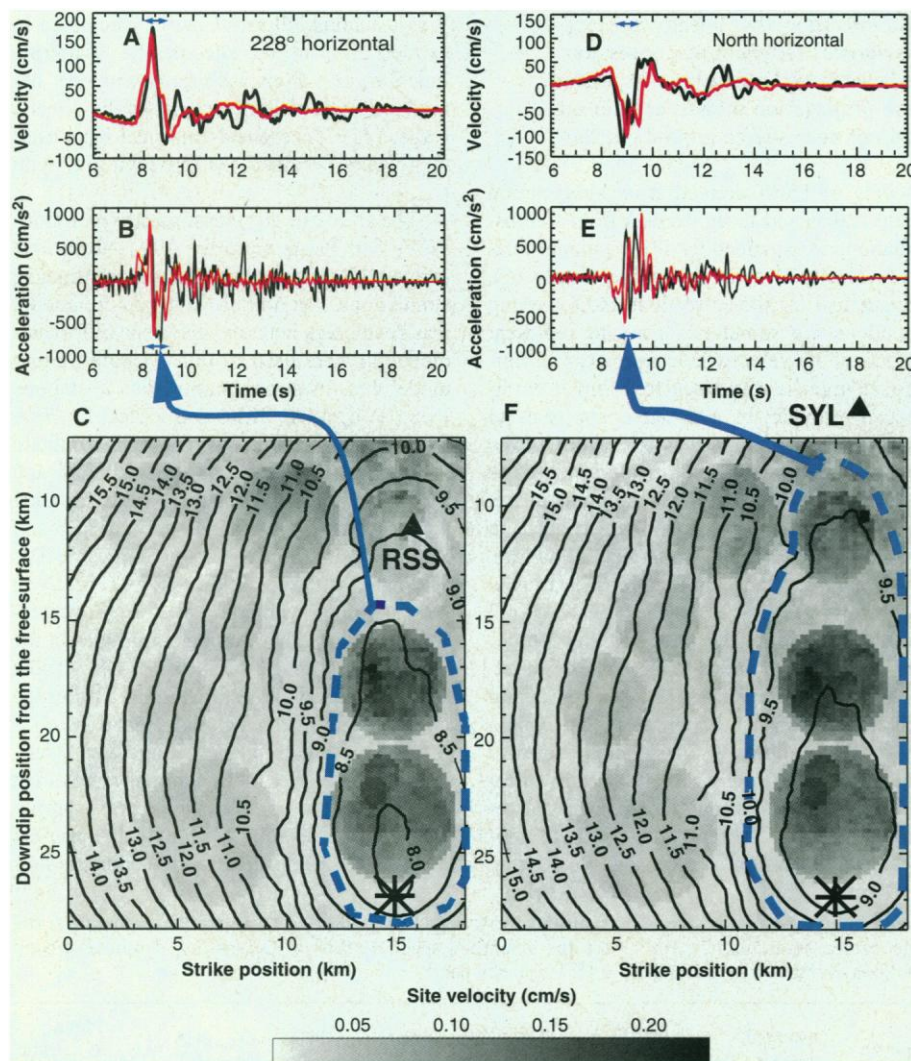


Fig. 1. Observed (black lines) and synthetic (red lines) maximum horizontal Northridge ground motions for RSS (A and B) and SYL (D and E). Line contours are the projection of  $S$ -wave rupture isochrones for RSS (C) and SYL (F) onto the buried fault plane (perspective is normal to the plane). Gray shading shows site-specific velocity contributions that include radiation patterns and geometric spreading. Dashed blue contours (C and F) show the large portions of the fault containing high-effective stress asperities (dark regions) that combine to produce the large joint PHVs and PHAs in the short time intervals (rupture directivity) shown by blue arrows in (A), (B), (D), and (E). Triangles show station positions above the fault. Each star is the hypocenter.

Ranges of southern California that are characterized by short wavelength deformation (23) and represent the limits of resolution for current 3D crustal velocity inversions (24). Random 3D fractal variations were applied to 1D hard rock, soft rock, and alluvial velocity models (Fig. 3) for 3D finite-difference calculations to investigate the ground-motion effects of propagation through the upper 5 km of 3D randomized southern Californian velocity-depth profiles.

The nonlinear site amplification hypothesis for Northridge alluvial sites (9, 10) is based on the assumption that wave propagation effects are similar for the mainshock and the aftershocks and therefore should not affect the aftershock-to-mainshock amplification ratios. Finite-difference calculations show that, in the presence of relatively small ( $\sigma = 5\%$ ) random 3D upper crustal velocity variations, linear wave propagation produces path effects proportional to magnitude.

PHAs and PHVs at near-source sites are produced by direct *S* waves that are radiated from the fault surface during earthquake rupture (25) (Fig. 1). Large PHVs and PHAs at near-source Northridge sites are produced by direct *S* waves radiated over large areas (25 to 40 km<sup>2</sup>) of the fault surface that sum together at these sites in short time intervals (~0.5 s; Fig. 1, C and F). Relative to smaller aftershocks, mainshock direct *S* waves traverse large cross sections of the crust as they propagate to and sum together at near-source sites. Conversely, the direct *S*-wave propagation cross sections for *M* 3 to 4 aftershocks, which produce most of the aftershock/mainshock amplification ratios in (9), are relatively small. For example, 10-MPa *M* 3 and *M* 3.7 aftershocks have rupture areas of 0.04 and 0.2 km<sup>2</sup>, respectively. Thus, aftershock direct *S*

waves summed at a particular site traverse a much smaller volume of 3D random crustal velocity variations than mainshock direct *S* waves. Mainshock direct *S* waves sample a much wider range of crustal heterogeneity than aftershock direct *S* waves, so phase complexity may reduce the coherence of mainshock direct *S* wave sums over short time intervals, reducing mainshock amplifications relative to aftershock amplifications. With the geometry shown in Fig. 2, this hypothesis was tested by determining how constructively free-surface synthetic seismograms sum over areas corresponding to typical aftershock and mainshock direct *S*-wave propagation cross sections in the upper crust (26).

The alluvial velocity model synthetic aftershock-to-mainshock PHA ratios reproduced the observed distribution of Northridge aftershock-to-mainshock amplification ratios at 13 of 15 sediment sites (Fig. 4). There is apparent misfit with the two largest observed amplifications. However, the mainshock and aftershocks were recorded at locations 100 m apart (inside and outside a building) for the second largest observed amplification (9), and there is a 0.54 probability that a large amplification ratio consistent with the upper 5% of the synthetic distributions would be observed in a sample size of 15. Thus, a linear wave propagation mechanism provides a viable alternative explanation of observed mainshock deamplification at alluvial sites during the Northridge earthquake. Linear 3D heterogeneous wave propagation and nonlinear soil responses are viable explanations of Northridge mainshock deamplification at alluvial sites; they are not mutually exclusive. Both mechanisms could occur to some extent and reproduce the observed aftershock-to-mainshock amplification ratios. However, if linear wave propagation through weakly random, heterogeneous 3D media is the dominant effect,

*M* > 6 earthquakes may be capable of producing larger PHAs at alluvial sites than observed during the Northridge earthquake. This could occur if alluvial sites are located in regions of maximum directivity for future earthquakes because direct *S*-wave summation cross sections could be smaller for some source-site geometries than occurred during the *M* 6.7 Northridge earthquake. If nonlinear soil responses dominate, PHA will not exceed threshold values determined by the soil properties. Resolution of which mechanism is dominant is critical to quantifying seismic hazards at alluvial sites located close to faults that produce *M* > 6 earthquakes.

Comparable 3D velocity randomizations produced larger aftershock-to-mainshock amplification ratios with the alluvial velocity model than with the soft rock or hard rock models. Likely mechanisms are (i) increased *P*-*SV* coupling (27) and (ii) increased direct *S*-wave travel-time variations. In the 3D alluvial velocity model, strong vertical velocity gradients increase *P*-*SV* coupling, which increases the rate of conversion of *P* to *S* and *S* to *P* and increases the conversion rate between forward and backward propagating *P* and *S* waves (28). Thus, for the alluvial velocity model, *P*-*SV* coupling, relatively higher attenuation, and frequency-dependent *S*-wave velocities (6) disperse the direct *S* wave's energy and increase its phase

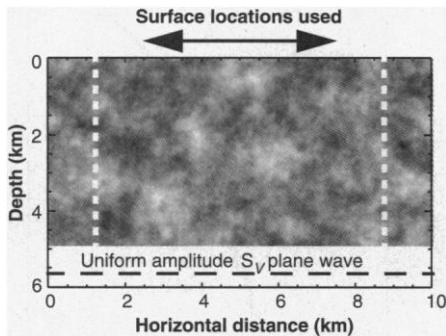


**Fig. 2.** Two-dimensional depth slice of the model geometry for the 3D finite-difference calculations. A uniform-amplitude *SV* plane wave (dashed black line) is introduced in the middle of a 1-km-thick homogeneous layer at the bottom. Only the inner 5 km by 5 km region of surface positions was used to avoid absorbing boundary artifacts (double arrow). A 10 km by 10 km model was used for the hard rock velocity model, and 7.5 km by 7.5 km models (limits shown as dashed white lines) were used for the soft rock and alluvial velocity models (Fig. 3). Gray shading shows the fractal velocity randomization pattern.

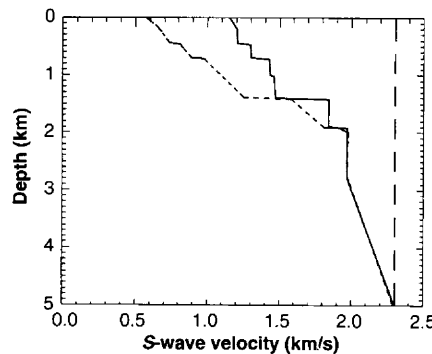


**Fig. 3.** Hard rock (long-dashed line), soft rock (solid line), and alluvial (short-dashed line) *S*-wave depth-velocity profiles for southern California (17). Corresponding *P*-wave velocities were obtained with *P*-to-*S* velocity ratios ( $V_p/V_s$ ) of 1.73 for the hard rock velocity model and  $V_p/V_s = 1.85$  at the surface tapered to  $V_p/V_s = 1.73$  at 2-km depth for the soft rock and alluvial velocity models.

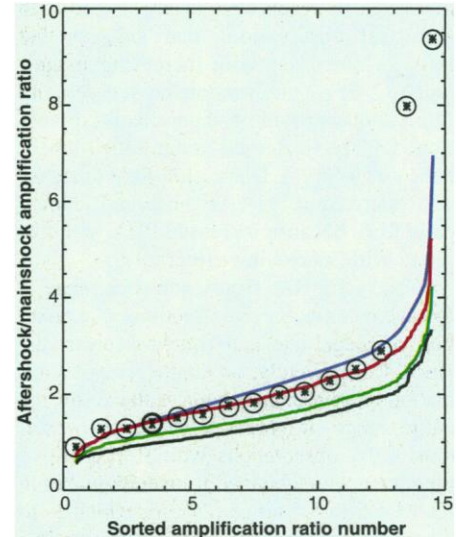


**Fig. 4.** Sorted observed alluvial site Northridge aftershock-to-mainshock amplification ratios at 3 Hz (stars in circles) from (9). The curves show sorted linear-elastic 3D finite-difference PHA < 4 Hz amplitude ratios of small aftershock summation cross sections to mainshock ~0.5-s isochrone interval summation cross sections. The alluvial velocity model curves (blue for *M* 3 0.04 km<sup>2</sup> sums/25 km<sup>2</sup> sums and red for *M* 3.7 0.2 km<sup>2</sup> sums/25 km<sup>2</sup> sums and *M* 3 0.04 km<sup>2</sup> sums/6.25 km<sup>2</sup> sums) reproduce 13 of the 15 observed ratios. The soft rock (green) and hard rock (black) velocity model curves represent *M* 3.7 0.2 km<sup>2</sup> sums/25 km<sup>2</sup> sums.

complexity. Lower near-surface velocities in the alluvial velocity model increase direct *S*-wave travel-time differences between locally low- and high-velocity regions, further reducing the phase coherence of the direct *S*-wave summation, particularly for shorter periods ( $T < 1$  s) that impact stiff structures such as dams and small steel frame and masonry buildings.

### Observed Log-Normal Distribution of PHA

The standard deviation of the natural logarithm of PHA [ $\ln(\sigma_{\text{pha}})$ ], expressing the random variability of ground motions, is a critical parameter influencing probabilistic seismic hazard assessments (PSHA). In western North America, observed values of  $\ln(\sigma_{\text{pha}})$  range from 0.5 to 0.7 (29). PHA dispersion is a consequence of source variability and wave propagation complexity, including whole-path and near-surface effects. The wave propagation contribution to  $\ln(\sigma_{\text{pha}})$  is evaluated with the soft rock model (Fig. 3) and the geometry shown in Fig. 2, values of  $a = 1$  km and  $\sigma = 5\%$ , and five propagation cross sections (30). Starting with vertically incident, uniform-amplitude *SV* plane waves, propagation through 5 km of random fractal 3D velocity fluctuations produces log-normal distributions of PHA (Table 2) (31). PHA dispersion is reduced as summation cross sections are increased, a result that is consistent with empirical observations that suggest that  $\ln(\sigma_{\text{pha}})$  decreases with increasing magnitude (32, 33). Thus, random crustal velocity fluctuations provide a theoretical explanation for the observed magnitude dependence of  $\ln(\sigma_{\text{pha}})$ . Dispersion may decrease with increasing PHA, as observed empirically (33), because increased PHA will correlate with increasing directivity.

Observed PHAs represent a wide range of *S*-wave summation cross sections as a function of magnitude and source-receiver distance. Consequently, no single *S*-wave summation cross section is representative for the entire range of observed PHAs. However, most PHA observations within  $\sim 20$  km of the source were obtained from earthquakes in the  $M$  5.5 to 6.7 range (29), for which 1- to 5-km<sup>2</sup> *S*-wave summation cross sections are a

reasonable analog for directivity regions (34). For these cross-section dimensions, about half (0.25 to 0.3) of the total observed PHA  $\ln(\sigma_{\text{pha}})$  dispersion (0.5 to 0.7) in western North America can be explained by  $\sigma = 5\%$  random 3D velocity variations in the upper crust.

Truncation of the upper tail of the log-normal approximation to PHA during PSHA has become recent practice (35). Unfortunately, for annual exceedence frequencies  $< 10^{-3}$ , PSHA are most sensitive to the upper tail of PHA distributions, which are based on sparse empirical observations. Consequently, selection of the truncation limit is somewhat arbitrary. A synthetic PHA distribution departs from its log-normal approximation near the upper tail of the distribution (Fig. 5), and the departure becomes more pronounced as the *S*-wave summation cross section increases. Random velocity fluctuations combined with an upper-frequency limit imposed by attenuation ( $f_{\text{max}}$ ) provide a regularizing mechanism that limits the growth of PHA at the upper tail of the distribution. This provides some physical support to the practice of truncating and renormalizing log-normal PHA attenuation relations for use in PSHA. However, it is necessary to acquire additional observational constraints on correlation lengths and scaling of random velocity variations to quantify the limits imposed on PHA by wave propagation through a 3D heterogeneous crust. Because rupture variability is also required to explain about half of the observed PHA dispersion, quantifying the appropriate cumulative frequency truncation points will require improved understanding of earthquake rupture dynamics and the associated variability of seismic wave radiation from faults.

Current crustal 3D velocity models developed to locate hypocenters do not resolve velocity variations with wavelengths of less than 2 to 5 km (24). The value of acquiring the information necessary to resolve finer scale deterministic 3D velocity structure is twofold: (i) As  $a$  is decreased, PHV and PHA prediction dispersion is reduced over a broader frequency band of engineering interest, and (ii) PHV and PHA biases associated with deterministic 3D velocity structure, such as low-velocity basins, can be more accurately

predicted over a broader frequency band of engineering interest with 3D ground-motion simulations (36).

### Implications for Near-Source Ground Motions

Heaton *et al.* (2) demonstrated that near-source ground motions could seriously damage high-rise flexible-frame buildings. However, the deterministic synthetic wave propagation approaches used in (2, 3) are not adequate to quantify how large PHV and PHA may become near faults. For most sites in the western United States, it is probably inappropriate to use deterministic  $G_{1D}$  synthetic ground motions to evaluate dynamic responses of both long-period ( $T > 1$  s) and short-period ( $T < 1$  s) structures; long-period PHVs can be overestimated, and short-period PHVs, which can be substantial for thrust and reverse faults, cannot be reliably predicted with  $G_{1D}$  responses. Realistic deterministic and statistical models of 3D crustal velocity variations are necessary to estimate short-period responses from future earthquakes. Knowledge of the scaling of long- and short-period near-source PHVs and PHAs is needed to make realistic assessments of the relative risks associated with flexible and stiff structures and to effectively reduce earthquake risks with finite resources.

Evidence for  $M > 7$  reverse-faulting earthquake sources in metropolitan Los Angeles (37) demonstrates the need to quantify long-period PHVs associated with  $M > 7$  earthquakes. Theoretical investigations of dynamic rupture for dipping faults show that reverse faults radiate particle velocities on portions of the hanging wall near the free surface up to a factor of 2 greater than those

**Table 2.** Soft rock model synthetic PHA dispersion-summation cross-section relations (31). The K-S quantities are described in (31).

Summation cross section (km <sup>2</sup> )	$\ln(\sigma_{\text{pha}})$	K-S statistic	K-S probability	Number of seismograms
0.05 × 0.05	0.49	0.016	> 0.99	10,000
0.195 × 0.195	0.47	0.025	> 0.99	1,600
0.45 × 0.45	0.45	0.035	0.96	400
0.95 × 0.95	0.34	0.06	0.99	100
2.45 × 2.45	0.21	0.19	0.91	16

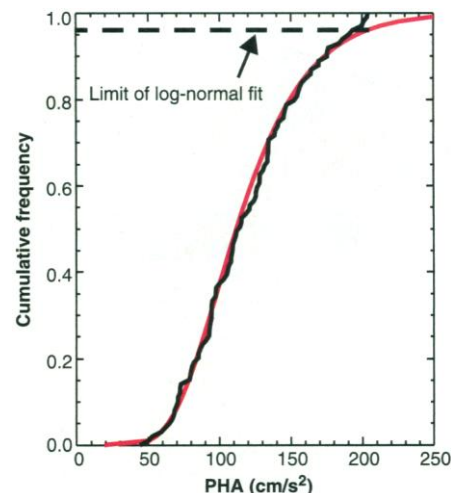


**Fig. 5.** Synthetic PHA dispersion (black curve) from the  $\sim 1$ -km<sup>2</sup> summation cross sections and the best fitting log-normal approximation (red curve). The dashed line shows the cumulative frequency limit for the fit of the log-normal approximation to the synthetic PHA distribution.

of normal faults (38). Deterministic and statistical 3D velocity variations in the upper crust must be accounted for to synthesize realistic free-surface PHVs and PHAs for sites located in the near-source region of reverse faults. Resolution of the appropriate PHVs and ground-motion durations (36) to use close to faults is necessary to engineer the correct proportion of load-bearing versus damping elements to ensure acceptable structural performance.

It is important to pursue 3D finite-difference investigations to determine what range of  $n$  values in Eq. 1 reproduce observed coda amplitudes and durations in the  $0.1 \text{ s} < T < 4 \text{ s}$  range of engineering interest. Estimates of  $n$ ,  $a$ , and  $\sigma$  as a function of depth and region are needed to quantify the scaling and variability of PHV and PHA, particularly near faults. For instance, PHV and PHA may be substantially higher in regions that have smaller random velocity variations than western North America, such as the central and eastern portions of the United States and Canada. New high-density installations of three-component broadband weak motion instrumentation are necessary to acquire sufficient  $S$ -wave travel-time and waveform data to reduce the correlation length of unresolved velocity variations.

#### References and Notes

- N. A. Abrahamson and W. J. Silva, *Seismol. Res. Lett.* **68**, 94 (1997); D. M. Boore et al., *ibid.*, p. 128; K. Sadigh et al., *ibid.*, p. 180; P. Spudich et al., *ibid.*, p. 190.
- T. H. Heaton, J. F. Hall, D. J. Wald, M. W. Halling, *Science* **267**, 206 (1995).
- J. G. Anderson and G. Yu, *Bull. Seismol. Soc. Am.* **86**, S100 (1996).
- "Correlated-random" means that random velocity fluctuations are dependent on surrounding velocities, with the dependence being inversely proportional to distance. Smoothness increasing with distance as  $a$  increases in Eq. 1, and overall smoothness is proportional to  $n$  in Eq. 1. This is a more realistic model of spatial geologic material variations than completely uncorrelated, spatially independent, random velocity variations. "Correlated-random" is shortened to "random" for the remainder of this paper.
- A. Frankel and R. W. Clayton, *J. Geophys. Res.* **91**, 6465 (1986).
- M. Roth et al., *Geophys. J. Int.* **115**, 552 (1993).
- J. W. Schneider et al., *Earthquake Spectra* **9**, 251 (1993); Y. Zeng et al., *Geophys. Res. Lett.* **22**, 17 (1995).
- L. Hutchings, *Bull. Seismol. Soc. Am.* **84**, 1028 (1994).
- E. H. Field et al., *Nature* **390**, 599 (1997); *J. Geophys. Res.* **103**, 26869 (1998).
- E. H. Field et al., *Seismol. Res. Lett.* **69**, 230 (1998).
- The 1D velocity-density model was derived from a 1D progressive velocity-hypocenter inversion with 97 stations and 183 earthquakes in the western Transverse Ranges, seismic reflection and refraction results [B. Keller and W. Prothero, *J. Geophys. Res.* **92**, 7890 (1987)], proprietary seismic reflection data, and cross-hole data at the site near Casitas Dam [P. C. Sirles and A. Viksnes, in *Geotechnical and Environmental Geophysics*, vol. III, *Geotechnical*, S. H. Ward, Ed. (Society of Exploration Geophysicists, Tulsa, OK, 1990), pp. 121–123]. Surface ( $\sim 250 \text{ m/s}$ ) and subsurface shear-wave velocities are similar to other alluvial sites in southern California [C. J. Wills, *Seismol. Res. Lett.* **69**, 216 (1998)]; D. M. Boore and L. T. Brown, *ibid.*, p. 222; ROSRINE project, <http://rccg03.usc.edu/rosrine>, J. P. Bardet, Ed., University of Southern California]. Deterministic  $G_{1D}$  functions were calculated with frequency-wave number integration [R. Kind, *J. Geophys.* **44**, 603 (1978)] to a minimum period of 0.1 s.
- O. Yilmaz, *Seismic Data Processing* (Society of Exploration Geophysicists, Tulsa, OK, 1987).
- Station naming convention is from D. Wald et al. [*Bull. Seismol. Soc. Am.* **86**, S49 (1996)]. The rupture model of Y. Zeng and J. G. Anderson (*ibid.*, p. 571) was used to construct an initial rupture model with eight asperities. The kinematic model of finite fault rupture uses fractal randomizations of effective stresses and rupture and healing velocities over the fault surface. These randomizations are combined with variable, high-effective stress circular asperities roughly consistent with (19, 20). Variable effective stress asperities provide the dominant short-period component of seismic energy. Perimeter transition regions smoothly decrease effective stresses from the asperity interiors to fault background regions and also allow for abrupt changes in local rupture and healing velocities. Rupture and healing velocities and effective stresses are independently specified for asperity interiors. Asperities are allowed to heal from their transition regions inward. Background regions of the fault that are far from healing boundaries (fault edges) can have substantially longer rise times. This allows for quite heterogeneous distributions of rise time on the fault, consistent with the results of (39, 40). Short rise times in the asperities provide large-amplitude, short-period radiation consistent with observations of relatively short rise times for rupture models of large earthquakes [T. H. Heaton, *Phys. Earth Planet. Inter.* **64**, 1 (1990)]. Longer rise times in the lower effective stress background region provide sufficient additional seismic moment to produce total moments consistent with observed broadband magnitudes [S. Horton, *Bull. Seismol. Soc. Am.* **86**, 122 (1996)]. Synthetic ground motions are calculated with point-source summation. Deterministic  $G_{1D}$  functions are calculated at 100-m depth and 150-m distance intervals, and the tau-p frequency-domain distance interpolation method of M. Henry et al. [*Geophys. Res. Lett.* **7**, 1073 (1980)] is used to obtain  $G_{1D}$  at required source-receiver distances. One of the nine scattering functions is chosen at random and applied to the appropriate  $G_{1D}$  at each point-source integration position to produce  $G_{\text{site}}$ . A 2D velocity model with fast velocities located between 15- and 20-km depth was used to approximate 3D  $S$ -wave travel-time variations consistent with (24).
- The ability of the Casitas Dam site scattering functions to reproduce PHV and PHA at other sites reflects the similarity of shallow velocity structure at these sites (11).
- S. P. Jarpe and P. W. Kasameyer, *Bull. Seismol. Soc. Am.* **86**, 1116 (1996).
- The rupture model consists of a 30-km-long fault dipping  $55^\circ$  from the surface to a depth of 20 km. Hypocenters are allowed to occur on 1-km intervals from 11- to 18-km depth and at 10 equally spaced locations along strike, producing 80 hypocenter positions. Eight asperity models are used to produce a total of 640 rupture models of a M 6.9  $70^\circ$  rake earthquake. The ground-motion site is located 3 km from the fault tip on the hanging wall and is 6 km from one end of the fault. Three fractal 2D velocity models are used to generate  $S$ -wave travel-time variations, which are used to time shift  $G_{\text{site}}$  and produce 1920 synthetic ground motions. The same 640 rupture models are used with  $G_{\text{site}}$  and  $G_{1D}$  [D. R. H. O'Connell, *Ground Motion Evaluations for Casitas Dam* (U.S. Bureau of Reclamation Seismotectonic Report 98-6, U.S. Bureau of Reclamation, Denver, CO, 1998)].
- G. Yu et al., *Bull. Seismol. Soc. Am.* **85**, 31 (1995).
- Single-scattering theory is valid when the mean free paths of the waves between the scatterers are greater than the travel distances from the scatterers to receivers. In the near-source region, these conditions are not satisfied, and multiple-scattering theory, which includes the effects of higher order scattering, is necessary [K. Aki, *Bull. Seismol. Soc. Am.* **82**, 1969 (1992); Y. Zeng, *ibid.* **83**, 1264 (1993)].
- D. J. Andrews, *J. Geophys. Res.* **85**, 3867 (1980); *ibid.* **86**, 12821 (1981).
- A. Frankel, *J. Geophys. Res.* **96**, 6291 (1991).  $b$  is the rate at which earthquake occurrence decreases with increasing magnitude from the Gutenberg-Richter relation for earthquake occurrence,  $\log(N) = a - bM$ , where  $N$  is the number of earthquakes per unit time  $> M$  and  $a$  is the activity rate.
- A. T. Walden and J. W. J. Hosken, *Geophys. Prospect.* **33**, 400 (1985).
- R. W. Graves, *Bull. Seismol. Soc. Am.* **86**, 1091 (1996).
- J. Namsom and T. Davis, *Geology* **16**, 675 (1988); R. S. Yeats, *Nature* **366**, 299 (1993); G. J. Huftile and R. S. Yeats, *J. Geophys. Res.* **100**, 2043 (1995).
- E. Hauksson and J. S. Haase, *J. Geophys. Res.* **102**, 5423 (1997).
- P. Bernard and R. Madariaga, *Bull. Seismol. Soc. Am.* **74**, 539 (1984); P. Spudich and L. N. Frazer, *ibid.*, p. 2061; *ibid.* **77**, 2245 (1987).
- This process was approximated here by summing free-surface synthetic seismograms contained within square cross sections corresponding to M 3 and M 3.7 aftershocks (0.04 and 0.2  $\text{km}^2$ ) and the mainshock (6.25 and 25  $\text{km}^2$ ) and dividing by the total number of seismograms in each cross section. In this procedure, the summation of unity amplitude seismograms would produce amplitudes of 1 for completely constructive interference and 0 for completely destructive interference. Aftershock-to-mainshock PHA ratios were calculated for all combinations of aftershock and mainshock cross sections (Fig. 4). A fixed grid spacing of 50 m was used. Four 3D fractal randomizations were superimposed on the three crustal velocity profiles shown in Fig. 3 for a total of 12 finite-difference calculations. An ideal experiment would use uniform surface velocities to correspond to a particular site. The fractal randomization produces varying surface velocities. Peak amplitudes scale proportionally with local surface velocity, and this contributes erroneous additional amplitude variability. However, additional finite-difference calculations showed that +10% and -10% surface velocity variations tapered to 0 at 0.5-km depth produced PHA variations of <10% about the median surface velocity response for frequencies of up to 4 Hz for all three crustal velocity profiles considered. This effect amounts to <10% of the median amplitude of the aftershock/mainshock amplitude ratios for the alluvial velocity model and is not a significant factor. Grid dispersion limits the maximum frequency to 4 Hz for the alluvial velocity model.
- $P$ -SV coupling refers to the fact that a wave quantity such as SV is modified by loss to, or gain from, other components of wave motion, such as  $P$ , arising from the nature of the variation of elastic media properties with position.
- Density variations are small in all velocity models considered here and are neglected in this simplified, smoothly varying, 1D vertical velocity stratification analysis. Assuming small values of ray parameter,  $p$  (near-vertical incidence), the coupling coefficients for  $P$  to  $S$  and  $S$  to  $P$  conversion for vertical velocity gradients are proportional to  $\rho \partial_x \mu$ , where  $\mu$  is rigidity and  $\rho$  is density, and the coupling coefficients for transfer from upgoing to downgoing waves are proportional to  $\partial_x \mu / \mu + 0.5 \partial_x u / u$ , where  $u$  is  $P$ - or  $S$ -wave slowness [B. L. N. Kennett, *Seismic Wave Propagation in Stratified Media* (Cambridge Univ. Press, New York, ed. 2, 1985), pp. 53–54]. For phase conversions from  $P$  to  $S$  and  $S$  to  $P$ , the alluvial model coupling coefficients are more than two times larger in the top 1 km of the alluvial velocity model than in the soft rock velocity model. For conversions between upgoing and downgoing waves, the alluvial velocity model coupling coefficients are 5.5 times larger in the top 1 km of the model than in the soft rock velocity model. Consequently, the direct  $S$  waves become more dispersed in the alluvial velocity model and do not sum together as constructively as direct  $S$  waves in the soft and hard rock velocity models.
- N. A. Abrahamson and K. M. Shedlock, *Seismol. Res. Lett.* **68**, 9 (1997).
- The results of the soft rock calculations discussed in (26) were used here. The synthetic seismograms were low-pass filtered at a corner frequency of 8 Hz to eliminate grid dispersion and to produce frequency responses roughly consistent with  $f_{\text{max}}$  [T. C. Hanks, *Bull. Seismol. Soc. Am.* **72**, 1867 (1982)] for most California soft rock and alluvial sites.
- The cumulative PHA distribution is compared with the best fitting cumulative log-normal distribution

- with the Kolmogorov-Smirnov (K-S) test [W. H. Press *et al.*, *Numerical Recipes in FORTRAN: The Art of Scientific Computing* (Cambridge Univ. Press, New York, ed. 2, 1992), pp. 617–622]. Low probability values for the K-S statistic suggest that two cumulative distributions are significantly different. K-S probabilities  $>0.9$  (Table 2) for all summation cross sections show that random fractal velocity fluctuations produce log-normal distributions of PHA.
32. R. R. Youngs *et al.*, *Bull. Seismol. Soc. Am.* **85**, 1161 (1995).
  33. K. W. Campbell, *Seismol. Res. Lett.* **68**, 154 (1997).
  34. Direct *S* waves, which dominate PHVs and PHAs recorded from larger magnitude earthquakes, traverse increasingly larger cross sections of the crust associated with larger fault dimensions. The summation cross sections in Table 2 are a proxy for this process, but these calculations show that PHA dispersion decreases as direct *S* waves are summed over increasing propagation cross sections.
  35. R. K. McGuire, *Bull. Seismol. Soc. Am.* **85**, 1275 (1995); I. G. Wong and J. C. Stepp, *Probabilistic Seismic Hazard Analyses for Fault Displacement and Vibratory Ground Motion at Yucca Mountain, Nevada* (U.S. Department of Energy, Washington, DC, 1998).
  36. A. Frankel, *Bull. Seismol. Soc. Am.* **83**, 1020 (1993); R. W. Graves, *ibid.*, p. 1042; K. B. Olsen, R. J. Archuleta, J. R. Matarese, *Science* **270**, 1628 (1995); K. B. Olsen and R. J. Archuleta, *Bull. Seismol. Soc. Am.* **86**, 575 (1996).
  37. C. M. Rubin, S. C. Lindvall, T. K. Rockwell, *Science* **281**, 398 (1998).
  38. D. D. Oglesby, R. J. Archuleta, S. B. Nielsen, *ibid.* **280**, 1055 (1998).
  39. T. Mikumo and T. Miyatake, in *Seismic Strong Motion Synthetics*, B. A. Bolt, Ed. (Academic Press, New York, 1987), pp. 91–151; *Geophys. J. Int.* **112**, 481 (1993); E. Fukuyama and T. Mikumo, *J. Geophys. Res.* **98**, 6529 (1993).
  40. A. Herrero and P. Bernard, *Bull. Seismol. Soc. Am.* **84**, 1216 (1994).
  41. Support for this research was provided by the Dam Safety Program of the U.S. Bureau of Reclamation. L.

Johnson recommended an investigation of random velocity variation effects on ground motions. I thank two anonymous reviewers and J. Ake, R. Denlinger, H. Huyck, and U. Vetter for comments that substantially improved the manuscript; J. Ake, R. Archuleta, B. Bolt, R. Denlinger, B. Foxall, A. Frankel, L. Hutchings, C. Nicholson, D. Oglesby, and P. Spudich for discussions; B. Bolt for reviews of previous versions of the manuscript; B. Darragh, J. Steidl, W. Silva, and D. Wald for strong motion data; R. Graves for a 3D elastic finite-difference program; P. Spudich for isochrone software; L. Johnson for reflectivity software; D. Copeland for field assistance; C. Wood for data acquisition hardware and software; and the Casitas Water District for field access. Short-period data were provided by the Southern California Seismic Network, which is operated jointly by the Seismological Laboratory at Caltech and the U.S. Geological Survey, Pasadena. L. Wald kindly provided instrument response information.

16 October 1998; accepted 22 January 1999

# Unconditional Security of Quantum Key Distribution over Arbitrarily Long Distances

Hoi-Kwong Lo<sup>1\*</sup> and H. F. Chau<sup>2</sup>

Quantum key distribution is widely thought to offer unconditional security in communication between two users. Unfortunately, a widely accepted proof of its security in the presence of source, device, and channel noises has been missing. This long-standing problem is solved here by showing that, given fault-tolerant quantum computers, quantum key distribution over an arbitrarily long distance of a realistic noisy channel can be made unconditionally secure. The proof is reduced from a noisy quantum scheme to a noiseless quantum scheme and then from a noiseless quantum scheme to a noiseless classical scheme, which can then be tackled by classical probability theory.

The art of secure communication—cryptography—has a long history. Before two parties can communicate securely, they often must share a secret random string of numbers (a key) for encryption and decryption. The secrecy of the message depends on the secrecy of the key. A problem in conventional cryptography is the key distribution problem: In classical physics, there is nothing to prevent an eavesdropper from monitoring the key distribution channel passively, without being caught by the legitimate users.

Quantum key distribution (QKD) (1–5) has been proposed as a solution to the problem. The quantum no-cloning theorem states that it is impossible to make an exact copy of an unknown quantum state (6). Thus, it is generally thought that eavesdropping on a quantum channel will almost surely produce detectable disturbances. The two users can,

therefore, use part of their quantum signals to test for eavesdropping. Only when the error rates are acceptable will they use the quantum signals to generate a key. Thus, the two users (commonly called Alice and Bob) have the confidence that if an eavesdropper (commonly called Eve) has a nonnegligible amount of information on the final key, she will almost surely be caught, even if she has infinite computing power and access to a quantum computer. Incidentally, several recent experiments have demonstrated the feasibility of QKD over tens of kilometers (7).

“The most important question in quantum cryptography is to determine how secure it really is” (8, p. 16). QKD is widely claimed to provide perfect security. However, this viewpoint has been under renewed scrutiny for two reasons. First, contrary to well-known claims of unconditional security (9), a class of other quantum cryptographic schemes, including so-called quantum bit commitment and quantum one-out-of-two oblivious transfer, has recently been shown to be insecure (10). Cheaters can defeat these schemes by a subtle application of the well-known Einstein-Podolsky-Rosen (EPR) paradox (11)

and by delaying their measurements. These “no-go” theorems not only shattered the long-standing belief in the security of those schemes, but they also undermined the confidence in QKD itself. Second, a convincing and rigorous proof of the security of QKD has been missing despite extensive investigations (12–15). Thus, the foundation of quantum cryptography has been shaky. Here, we solve this long-standing problem by proving that, given quantum computers, QKD can be made unconditionally secure over arbitrarily long distances.

A rigorous proof of the security of a QKD scheme requires the explicit construction of a procedure such that, whenever Eve’s strategy has a nonnegligible probability of passing the verification test by Alice and Bob, her information on the final key will be exponentially small (16–17). This procedure must be secure and efficient, even when Alice and Bob use imperfect sources and devices and share a noisy quantum channel.

Most analyses of the security of QKD have dealt with single-particle eavesdropping strategies (12), with immediate or delayed measurements, as well as the so-called collective attacks (13), in which Eve brings each signal particle into interaction with a separate probe system but then, after hearing the public discussion between Alice and Bob, measures all probes together. Security against the most general type of attack, the so-called joint attack, has been investigated by Deutsch *et al.* and also by Mayers. The discussion by Deutsch *et al.* was restricted to the special case of perfect devices (14). It introduced the concept of quantum privacy amplification, based on a process called entanglement purification, which was studied by Bennett, DiVincenzo, Smolin, and Wootters (BDSW) (18). Earlier versions of Mayers’s proof (15) have not been accepted as definitive. His most recent version of the proof is more detailed and complex (19). He proposes a proof of security of the Bennett and Brassard (BB84) (2) scheme against joint attacks in the presence

<sup>1</sup>Hewlett-Packard Laboratories, Filton Road, Stoke Gifford, Bristol BS34 8QZ, UK. <sup>2</sup>Department of Physics, University of Hong Kong, Pokfulam Road, Hong Kong, China.

\*To whom correspondence should be addressed. E-mail: hkl@hplb.hpl.hp.com